Flow characteristics of blade unit of a tridimensional rotational flow sieve tray under concurrent gas-liquid flow

Hongkai Wang[a], Meng Tang[*a,b], Dewu Wang[a], Yan Liu[a], Yishuo Zhang[a], Baisong Hu[a], Ruojin Wang[a], Shaofeng Zhang[*a]

a. School of Chemical Engineering and Technology, Hebei University of Technology, Tianjin 300401, China

b. School of Mechanical Engineering, Hebei University of Technology, Tianjin 300401, China

* Corresponding author. Tel.:+86 13132081566; +86 13920207743

Email address: 1986037@hebut.edu.cn (Shf. Zhang); mtang@hebut.edu.cn (M. Tang)

Graphical Abstract

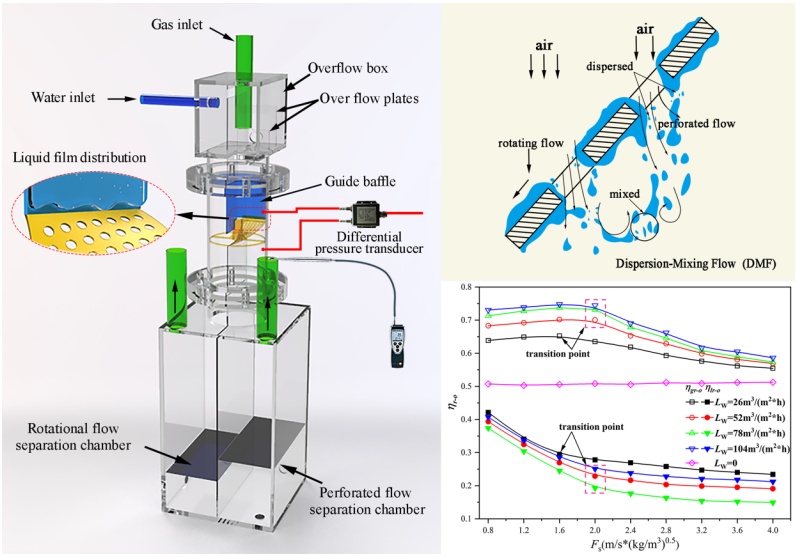

Abstract

The flow characteristics of the blade unit of a tridimensional rotational flow sieve tray was investigated experimentally in this study. First, the flow patterns are defined under different liquid arrangement methods. They are bilateral film flow, continuous perforated flow, and dispersion-mixing flow in overflow distribution and film and jet flow and jet and mixed flow in spray distribution. Second, the time and frequency domain analysis of the differential pressure pulsation signal in the blade unit is carried out. The influence of perforation and mixing intensity on the flow pattern transition is clarified. Third, the rotational flow ratio of the gas-liquid phase is measured. The influence of the operating conditions on the distribution of the rotational and perforated flow for the gas-liquid phase is investigated. Finally, a prediction model for the rotational flow ratio is proposed. The prediction results agree well with the experimental data.

Key words: Flow characteristics; Flow patterns; rotational-perforated flow; tridimensional rotational flow sieve tray; concurrent gas-liquid flow

1. Introduction

Unit operations, such as absorption, rectification, and catalytic oxidation, occur in columns, and columns are widely used in the chemical industry and refining and pharmaceutical production processes. The columns can be divided into packed and tray columns based on their internal structure [1,2]. A packed column is a type of differential contact equipment used for mass transfer. The internal components are fillers, which have the advantages of a low-pressure drop, high separation efficiency, simple structure, etc. The cost of the filler is high, and the plugging resistance of the packing is poor [3-5]. For graded contact equipment, the tray column has a large operating elasticity, low cost, and extensive applicability and can be fed on the side of the column. The core component of the tray column is the tray. The current mainstream trays are the sieve tray [6], bubble cap tray [7], and valve tray [8,9], which have a large processing capacity, excellent performance, and mature technology. Thus, the development of novel tridimensional trays has increased in recent years. This type of tray has a high mass transfer efficiency and large flux and can use the inner space for mass transfer. Representatives of this type of tray are the new vertical screen

plate [10], combined trapezoid spray tray [11], and flow-guided jet packing tray [12].

The contact method for the gas-liquid phase of the above-mentioned trays is mainly spraying contact, and a higher separation efficiency is required in flue gas desulfurization, dust removal, and absorption [13]. Among the numerous forms of gas-liquid contact, gas-liquid rotational flow is widely used in separation, mixing, and other operations [14,15]. Numerous scholars have conducted in-depth research on the rotatinal flow. Li et al. [16] studied gas-liquid flow in a vertical pipe containing a swirler with four helical vanes and classified three flow patterns by observation: rotational gas-liquid flow, rotational intermittent flow, and rotational annular flow. They also built a self-organizing neural network to identify the rotational flow regimes. In the double-alkali desulfurization process, Bao et al. [17] adopted a heterogeneous condensation technology using a rotating-steam tray to remove particles. The steam addition method improved the removal efficiency of the particles. K. H. Javed et al. [18] investigated rotational gas flow in a spray tower. The experimental investigations were based on the air–NH_3/H_2O system. The rotational flow in the gas phase enhanced the mass transfer coefficient up to 20%, compared to that in axial flows. However, although rotational flow for the gas-liquid phase increases the separation efficiency, a large amount of kinetic energy is lost in the process of fluid swirl, resulting in an increase in the pressure drop and corresponding energy consumption.

In addition to rotational flow, perforated flow is a common form of gas-liquid flow. For the sieve tray column, the gas-liquid phase perforates the sieve holes in a countercurrent method, which causes bubbling of the liquid layer on the sieve tray, and then produces constantly updated foam flow. Mass transfer occurs in the foam [19,20]. The perforated flow makes the gas-liquid contact more uniform, reduces pressure drop, and reduces energy consumption. Numerous researchers have studied the flow pattern characteristics of perforated flow. The gas-liquid concurrent downward flow through an orifice plate was experimentally investigated by Min et al. [21]. The trickling, continuous, semi-dispersed, and perfect-dispersed flows were defined by observation. The transition mechanism of the flow patterns was studied by the differential pressure pulsation method. A model for the film thickness around the orifice rim was also proposed. Maidana et al. [22] studied the air-water slug flow under the disturbance by an orifice plate in a horizontal tube. The results showed that the orifice disturbances have a significant influence on the void fraction, bubble nose velocity, and frequency of passage. For the orifice plate, Rahimi et al. [6] developed a 3-D two-phase CFD model to study sieve tray efficiency, hydraulics, and

mass transfer. Two types of sieve trays with different diameters were investigated using a simulation. The sieve plate with smaller sieve holes had a higher mass transfer efficiency when the flow pattern was close to the plug flow.

In addition, the operation mode of most trays is gas-liquid countercurrent flow, which has a higher mass transfer efficiency. However, when the gas volume reaches the upper limit of the tray load, flooding will occur, greatly reducing the mass transfer efficiency [23]. Concurrent flow can effectively avoid flooding and has a lower pressure drop than that of countercurrent flow. Therefore, the flux of the gas-liquid phase is higher, increasing the processing capacity and reducing the volume of the column equipment. For mass transfer, researchers have shown that, in the chemical absorption process or a low phase equilibrium constant, the concurrent flow has the same mass transferability as that of countercurrent flow [24]. Therefore, for chemical absorption, exhaust gas treatment, and plant exhaust desulfurization processes, the concurrent flow has the advantages of low energy consumption, high efficiency, and good economy.

In conclusion, there is a high spatial utilization rate for the tridimensional tray, a good separation effect of the rotational flow, and a low-pressure drop and high mass transfer of the sieve tray. Tang et al. proposed a novel tridimensional tray, referred to as the tridimensional rotational flow sieve tray (TRST) [25]. In Fig. 1, the TRST consists of several blades with a specific twist angle and internal and external support rings with even sieve holes on the blades. During operation, the internal flow pattern of the TRST can be divided into two flow modes: rotational flow and perforated flow. Rotational flow can enhance the turbulence intensity and mass transfer performance of the gas-liquid phase. The perforated flow enhances the fluid mixing between the adjacent rotational flow channels, shears and breaks the large bubbles or air masses, and further increases the contact area of the gas-liquid phase, enhancing mass transfer again. The TRST has no downcomer. It is a cross-flow tray, with a larger effective flow area. If used with the gas-liquid concurrent flow, the flux for the gas-liquid phase can be further enhanced, while the low-pressure drop is guaranteed, providing potential application in the field of flue gas desulfurization and dust removal [26].

Recently, a systematic study on the hydrodynamic properties of the TRST was performed by Tang et al. The experiment investigated the pressure drop and flooding of the tray under countercurrent and concurrent flow, respectively. The pressure drop was mainly affected by the flux for the gas-liquid phase, structures of the TRST, and installation

quantity and mode. Compared to countercurrent flow, no flooding occurred during concurrent flow, which has a lower pressure drop and a larger operating range. The gas and liquid volume range increased by at least 80% and 60%, respectively [27]. In addition, Tang investigated the internal gas flow field of the TRST using CFD technology and the distribution of axial, radial, and circumferential velocities in the TRST. The flow process of the gas-phase through the TRST was divided into the stages of initial and full development by distinguishing the direction of the gas-phase velocity. For different structures of the TRST, the rotational flow transition point was approximately 2/5 of the tray [28].

Although a preliminary understanding of the hydrodynamic properties of the TRST has been obtained, the key issues, such as the flow pattern, interaction intensity, and proportional distribution of the rotational and perforated flow for the gas-liquid phase, are not clearly understood. It is difficult to observe the internal flow field of the entire tray because the twisted blades block each other. Therefore, the research object is simplified, and the blade unit is extracted (see Fig. 1). The methods of experimental observation, photography, and differential pressure pulsation are combined to define and discriminate the flow patterns in the unit, and the gas-liquid phase interaction of each flow pattern is analyzed. A new experimental method is designed to measure the proportion distribution ratio of the gas-liquid phase rotational and perforated flow. The mechanism of rotational and perforated flow is analyzed, and a prediction model for the rotational flow ratio is proposed. The results of this study provide a theoretical foundation for the optimization of the structures of the TRST and mass transfer investigations for further research.

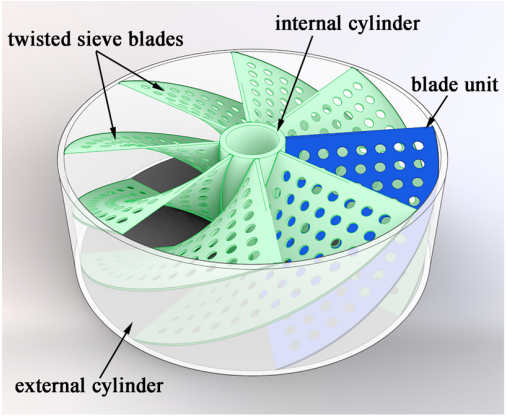

Fig. 1 Schematic diagram of TRST.

2. Experimental setup

The schematic diagram for observing the flow patterns is shown in Fig. 2. The apparatus is made of transparent acrylic resin to allow observation of the flow pattern. The experiments are conducted at room temperature and standard atmospheric pressure, and the air-water system is chosen in this experiment. The gas and liquid phase are transported to the spray box by a magnetic pump and blower, respectively. The liquid and gas phases flow through the channel of the blade unit. The guide plate eliminates the outside interferences. The sieve plate unit is positioned at the end of the baffle. The bottom of the unit is connected to the central bulkhead of the barrel section, which extends to the bottom of the water tank, dividing the tank into two parts. The rotational and perforated fluid are separated through a central separator. The swirling liquid enters the swirling separation chamber. The gas phase flows out through the left stoma outlet, and the perforated liquid flows into the perforated flow separation chamber. The perforated gas flows out through stoma outlet2. Heights h_{1r} and h_{2p} of the rotating flow and perforated flow can be read from the two separation chambers, and a hot-wire anemometer is located at the gas phase exits to measure the gas flow rate, u_{gr} and u_{gp}. The exit aperture is the same and known; therefore, the corresponding gas flow volume can be calculated based on the velocity. The pressure measuring points are set at 20 mm on both sides of the unit, and the pressure changes can be measured by the differential pressure sensor in real-time.

The liquid phase distribution is uneven on the unit surface owing to the liquid distributor when the liquid density is small, thereby disagreeing with the actual working conditions. Therefore, the overflow method of liquid distribution is adapted. As shown in Fig. 2b, the spray box is replaced by the overflow box. The liquid phase passes the box through two overflows and flows along the guide plate connected to the box after stabilization. The liquid phase flows to the upper edge of the blade unit in the form of falling film flow (as shown in Fig. 2b inside the ellipse). Then, the liquid phase is evenly laid on the surface of the unit, and the gas-phase inlets and other experimental conditions remain unchanged.

In this experiment, the diameter of the blade unit is 140 mm; the axial height is 50 mm; the overall height of the device is 1.2 m. The diameter of the cylinder section where the unit is located is 150 mm. The structure parameters and shematic of the blade unit are listed and

shown in Table 1 and Fig. 3.

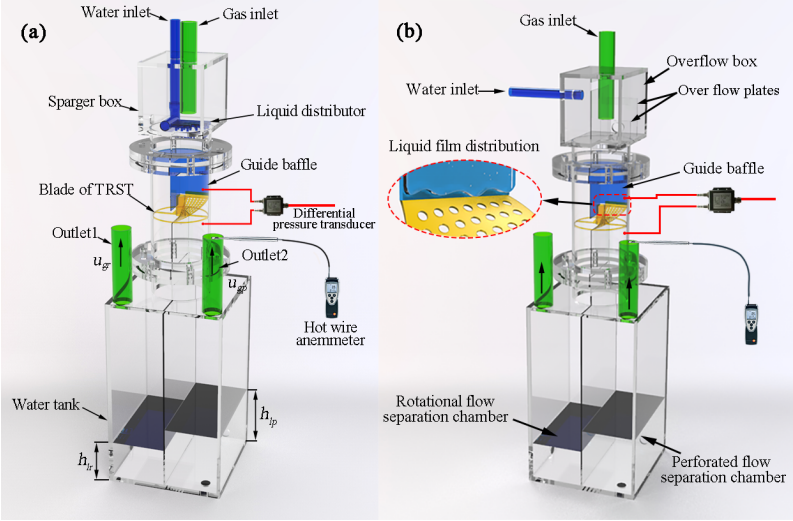

Fig. 2 Experimental apparatus. (a) Spary distribution; (b) Overflow distribution.

Table 1. Structure parameters of the blade unit

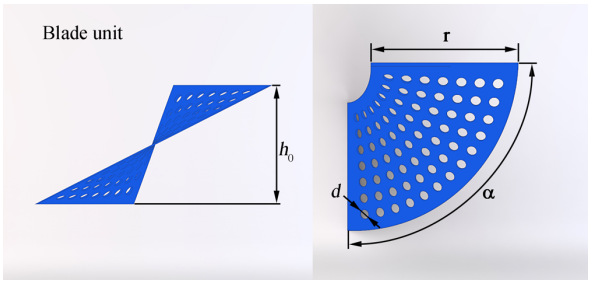

Fig. 3 Prameters of the blade unit

label	value
h_0 (mm)	50
r (mm)	74.5
α (°)	90
d (mm)	4
Number of sieve holes	70
Aperture ratio	0.243

3. Results and discussion

3.1. Flow patterns of the blade unit

The flow pattern and transformation of that under two types of liquid arrangement methods of the blade unit are discussed in this section. To compare the results with similar research, the gas and liquid quantities are characterized by the gas-phase kinetic energy factor (F_s) and the liquid-phase spray density (L_w). The liquid film is evenly distributed on the surface of the sieve plate unit under the overflow distribution; therefore, the liquid spray density is the same as that under the spray distribution. The kinetic energy factor of the gas phase and the spray density are calculated as follows:

$$F_s = u_g \sqrt{\rho_g} \tag{1}$$

$$L_W = \frac{L}{A} \tag{2}$$

Here, u_g represents the apparent velocity; L is the volume of the liquid phase; A is the area of the cross-section of the fluid, which equals $\pi r^2/4$. According to the experimental setup of Tang [25], the range of the operating conditions is determined: gas-phase kinetic energy factor: F_S: 0.4–4 (m/s*(kg/m^3)$^{0.5}$), gradient: 0.4 (m/s*(kg/m^3)$^{0.5}$); liquid spray density: L_W: 26–260 m^3/(m^2*h).

3.1.1. Flow patterns in overflow distribution

The liquid phase is dyed with rhodamine B solution to observe the flow patterns. Canon EOS 70D is used to take photos of the flow pattern. The exposure time is 1/4000 s, and the ISO is 3200. An LED spotlight (5MT-100W) is applied as a camera light source. Under the overflow distribution, the flow patterns of the blade unit can be defined as three types based on the characteristics of the rotational and perforated flow of the gas-liquid two-phase flow system. They are bilateral film flow (BFF), continuous perforated flow (CPF), and dispersed-mixing flow (DMF) under the spray distribution, and film and jet flow (FJF) and jet and mixed flow (JMF) under spray distribution.

3.1.1.1. BFF

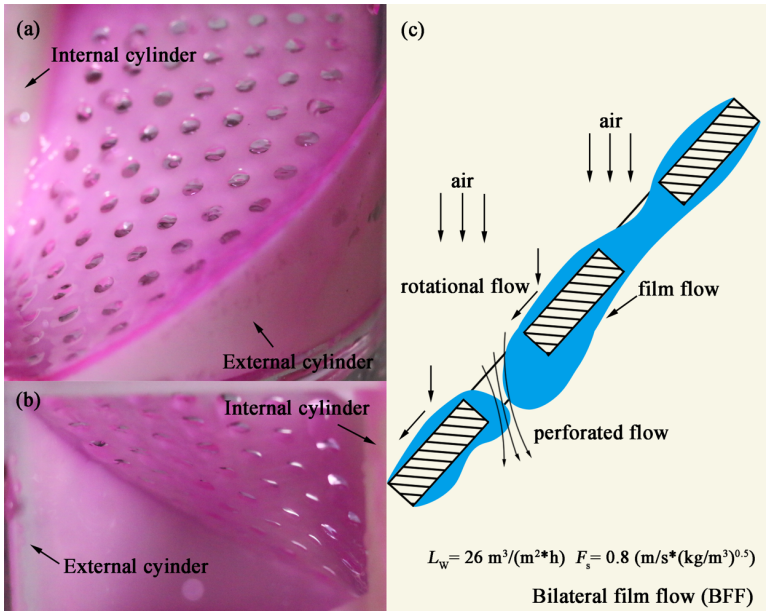

Fig. 4 Bilateral film flow. (a) The front side; (b) The reverse side; (c) Diagram of BFF.

Fig. 4 shows the flow pattern of BFF. The operating conditions are F_s = 0.8 (m/s*(kg/m^3)$^{0.5}$), L_W = 26 m^3/(m^2*h). As shown in Fig. 4a, the liquid phase flows to the upper edge of the blade unit under the guidance of the guide blade. Affected by gravity, the liquid slowly wets the surface of the blade unit under the guiding action and forms a thin and stable liquid film. Because of the liquid-phase surface tension, the sieve holes are covered with the liquid layer as well; however, with the combined effect of gravity and the driving force of the gas phase, the liquid film on the sieve hole will gradually sink and accumulate into small droplets. The film at the sieve hole will be broken by the airflow, creating a smaller gap. However, the kinetic energy factor is relatively small; thus, the gas cannot break the liquid layer. The droplets affected by the viscosity forces attach to the rear of the unit sieve edge and form a dispersed liquid film flowing down the back of the unit. At the same time, the sieve holes broken by the gas phase will be covered by the liquid film again, repeatedly.

3.1.1.2. CPF

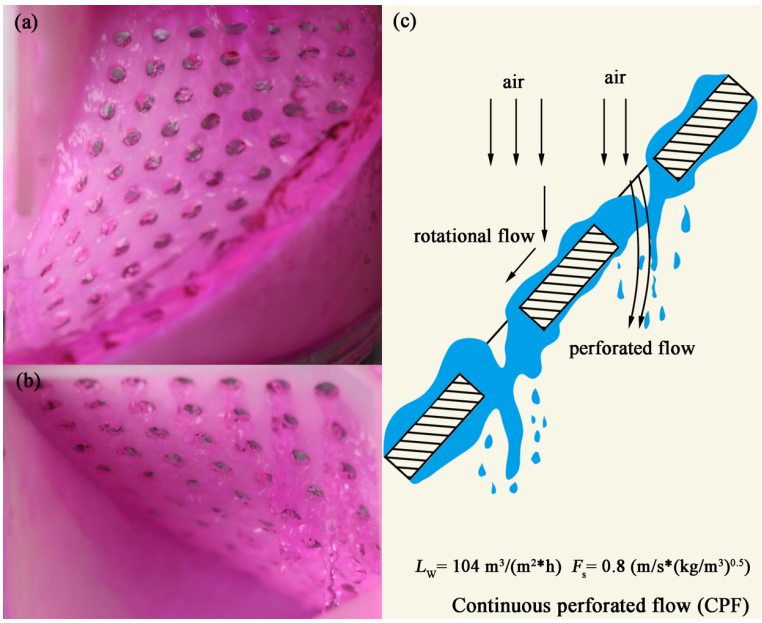

Fig. 5 Continuous perforated flow. (a) The front side; (b) The reverse side; (c) Diagram of CPF.

Fig. 5 shows the flow pattern of the CPF. The operating conditions are F_s = 0.8 (m/s*(kg/m^3)$^{0.5}$), L_W = 104 m^3/(m^2*h). As shown in Fig. 5a, the liquid spray density is increased. The liquid film on the surface and sieve holes of the blade unit is significantly thickened. With the centripetal and centrifugal force at the internal and external blade unit, the liquid film on the inside of the unit (near the inner cylinder) and outside of the unit

(near the outside cylinder) thickens and is thin in the middle. On the reverse side of the unit, continuous droplets and multiple streams flow through the sieve holes near the inner cylinder because the slope is large on the inside. The downward component of the velocity is increased. The liquid film thickens, and the cumulative mass increases simultaneously, which increases the flow velocity of the liquid film. The liquid cannot coat the sieve holes under the influence of surface tension. The liquid phase flows through the holes continuously. The slope of the middle and outer sides of the unit is smaller than that of the internal unit, and the downward component velocity is smaller. The flow rate of the liquid film decreases, and the influence of the surface tension becomes significant. The liquid film coats the sieve holes again and sinks and forms droplets that adhere to the back of the blade unit, presenting a dispersed fluid film flow. The flow mechanism is similar to that of the BFF.

3.1.1.3. DMF

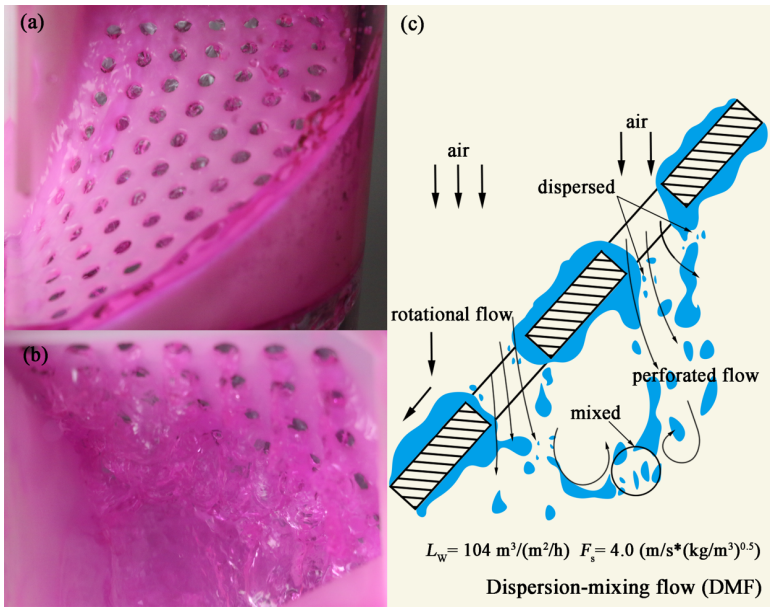

Fig. 6 Dispersion-mixing flow. (a) The front side; (b) The reverse side; (c) Diagram of DMF.

The flow pattern of DMF is shown in Fig. 6. The operating conditions are L_W = 104 $m^3/(m^2*h)$, F_s = 4.0 $(m/s*(kg/m^3)^{0.5})$. As shown in Fig. 6a, the gas kinetic energy factor reaches the maximum in the operating range. The gas-phase propulsion increases significantly. The liquid film accumulates towards the inner and outer edges of the unit, affected by the squeezing influence of the gas phase. The centripetal and centrifugal action caused by the unique structure of the unit create an uneven distribution on the unit surface. The liquid layer in the middle is thin and thick on both sides. A portion of the sieve holes is

covered by the liquid film, which has obvious depressions, and the other part of the screen is open, indicating that the liquid film has been broken by the airflow. On the back of the sieve plate unit, the droplet and liquid column flow out from the sieves at a high speed and mix with each other, see Fig. 6b. The fluid film at the sieve holes cannot resist the strong impact of the gas phase. The film is broken by the gas phase and forms small droplets, which mix with the airflow. A chaotic turbulence flow is eventually formed on the back of the unit.

3.1.2. Flow patterns in spray distribution

3.1.2.1. FJF

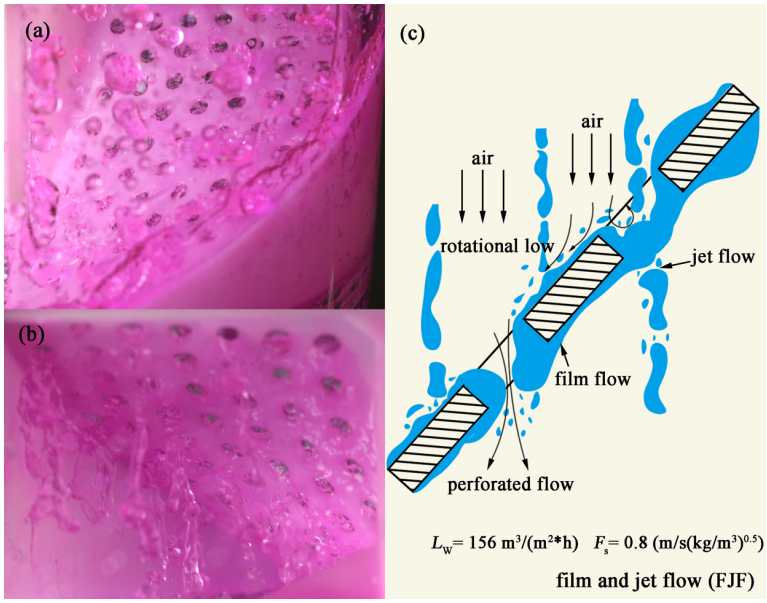

Fig. 7 Film and jet flow. (a) The front side; (b) The reverse side; (c) Diagram of FJF.

Spray liquid distribution has a larger spray density than that of the overflow liquid distribution. Fig. 7 shows the flow pattern of FJF. The operating conditions are L_W = 156 $m^3/(m^2*h)$, F_s = 0.8 $(m/s*(kg/m^3)^{0.5})$. The liquid phase sprays the plate unit surface through the tube-type liquid distributor. Because of the dispersed distribution of the liquid columns, most of the spray columns directly hit the surface of the unit and then spread out to form an uneven liquid film, as shown in Fig. 7a. Moreover, a small portion of the spray column hits the sieve area or flows through the holes directly. Other columns hit the edge of the holes, shearing into two parts. Columns with a larger vertical downward velocity component efflux from the sieve holes, while the ones with a larger horizontal velocity component gather on the liquid film on the surface of unit and spread continuously. Because of the high density of the liquid spray, the liquid film on the unit surface is thicker. With the influence

of gravity and the driving force of the gas phase, the liquid phase on the sieve holes not hit with the spray columns will gradually gather and flow in the form of liquid columns. Therefore, there is a continuous outflow at each sieve hole on the back of the unit. However, because of the low gas velocity, the liquid column is less disturbed by the gas phase, and the boundary is clear, see Fig. 7b.

3.1.2.2. JMF

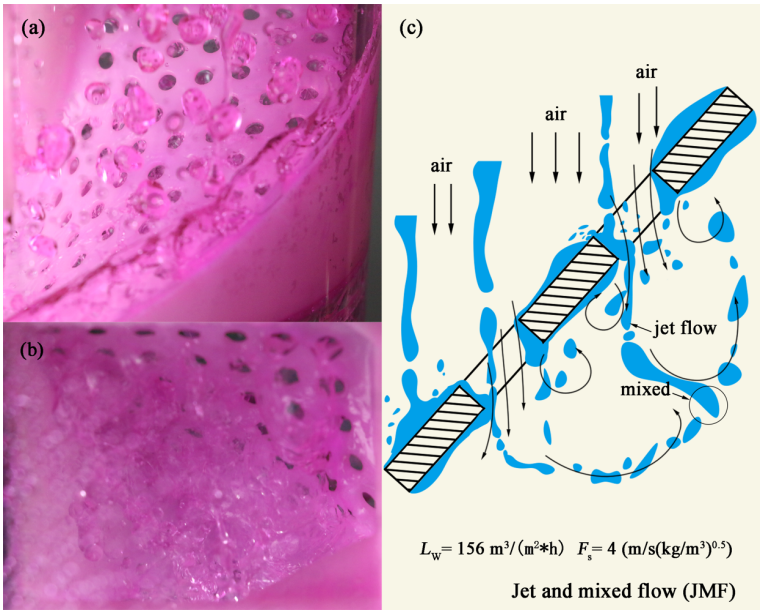

Fig. 8 Jet and mixed flow. (a) The front side; (b) The reverse side; (c) Diagram of JMF.

The flow pattern of the JMF is shown in Fig. 8. The operating conditions are L_W = 156 $m^3/(m^2*h)$, F_s = 4.0 $(m/s*(kg/m^3)^{0.5})$. The gas kinetic energy factor increases. The liquid film on the unit surface is blown away by the air jet stream, and the distribution becomes more unevenly distributed. As shown in Fig. 8b, the liquid phase blown out by the gas airflow at the back of the unit is ejected. The dispersed droplets and columns flow disorderly and mix. The flow mechanism of the flow pattern is similar to that of the DMF.

3.2. Interaction intensity and operating conditions for different flow patterns

First, the acquired differential pressure signal is processed to remove the singularity, and the moving average method is used to denoise the signal to obtain the time-domain characteristic diagram of the differential pressure signal [29]. Second, the Welch average period method, where the Hanning window is adapted is used to estimate the frequency

spectrum density (PSD) of the de-noised differential pressure signal [30]. Finally, combined with the domain signal and power spectrum density, the interaction intensity of the gas-liquid is analyzed, and the operating field under different liquid distributions of flow patterns can be divided [31].

3.2.1. Time-domain analysis for the pressure pulsation signal

Fig. 9 and Fig. 10 show the time domain signals of the differential pressure of all the flow patterns. The pressure signals of the gas phase in the time domain under overflow distribution are shown in Fig. 9a, and the liquid spray density is L_W = 78 $m^3/(m^2*h)$. With the increasing kinetic energy factor of the gas phase, the average amplitude of the pressure difference pulsation presents a stepped-upward trend. For the range of the kinetic energy factor of the gas phase $F_s \leq 1.2$(m/s*$(kg/m^3)^{0.5}$), the pulsation change in the pressure difference is stable. In this operating range, the flow pattern is a bilateral flow. The surface and sieve holes of the unit are covered by the liquid film. The gas phase mainly flows through the unit in the form of rotational flow. In this case, the gas velocity is low, and the interaction between the gas and liquid phases is weak; therefore, the pressure difference fluctuation is weak.

When the gas-phase kinetic factor F_s rises to 1.6 (m/s*$(kg/m^3)^{0.5}$), the pressure difference amplitude increases as the gas velocity increases, and the flow pattern of the unit starts to change into CPF, under the squeezing influence of the gas phase. At this time, the gas phase perforation is still hindered by the liquid layer at the sieve holes, and the proportion of the rotational liquid phase is large. Although the gas-liquid two-phase interaction is slightly strengthened, the overall gas velocity is relatively small, and the pressure difference fluctuation is stable. When the kinetic factor increases to F_s = 2.4 (m/s*$(kg/m^3)^{0.5}$), the gas phase propulsion becomes prominent, and the flow pattern changes from CPF to DMF. The liquid layer above the sieve holes is continuously blown out by the airflow and replenished immediately. The gas-liquid phase is mixed on the back of the unit. The interaction force between the two phases is increased, resulting in a sharp fluctuation in the pressure difference signal.

The time-domain signal changes of differential pressure pulsation are shown in Fig. 9b. The liquid spray density is L_W = 156 $m^3/(m^2*h)$. The pulsation amplitude of the differential pressure signal gradually increases with the increasing gas-phase kinetic energy factor, which is similar to that under the overflow distribution. The flow pattern changes into the

FJF when the gas phase kinetic energy factor $F_s \leq 1.6$ (m/s*(kg/m^3)$^{0.5}$). At this point, the gas-phase velocity is small, and the influence of the gas phase decreases. The regular jet flow of the liquid is dominant on the reverse side of the unit, and the mixing degree of gas-liquid is low. The fluctuation of the differential pressure signal is stable.

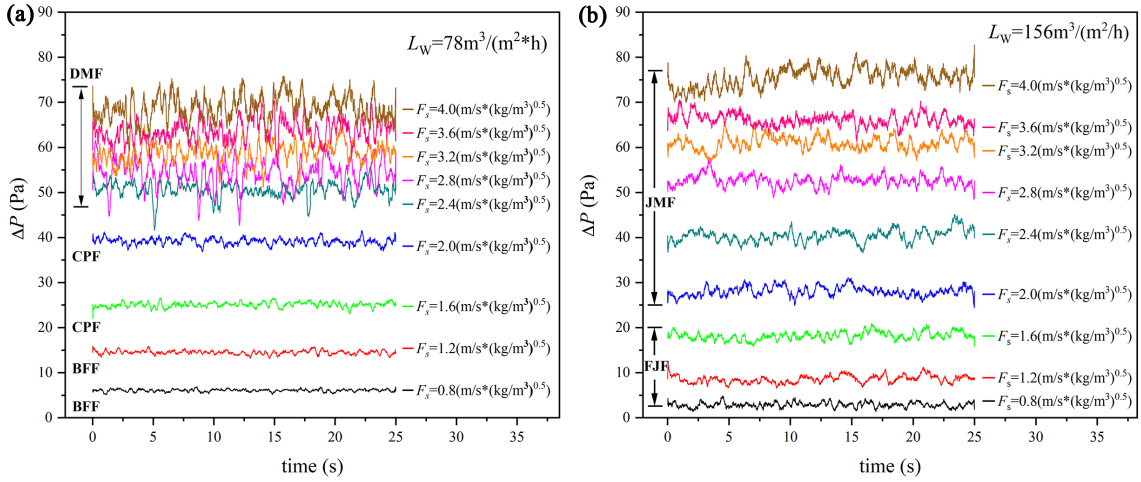

Fig. 9 Time-domain diagram of differential pressure pulsation under different gas-phase kinetic factors. (a) L_W = 78 m^3/(m^2*h) in overflow distribution; (b) L_W = 156 m^3/(m^2*h) in spray distribution.

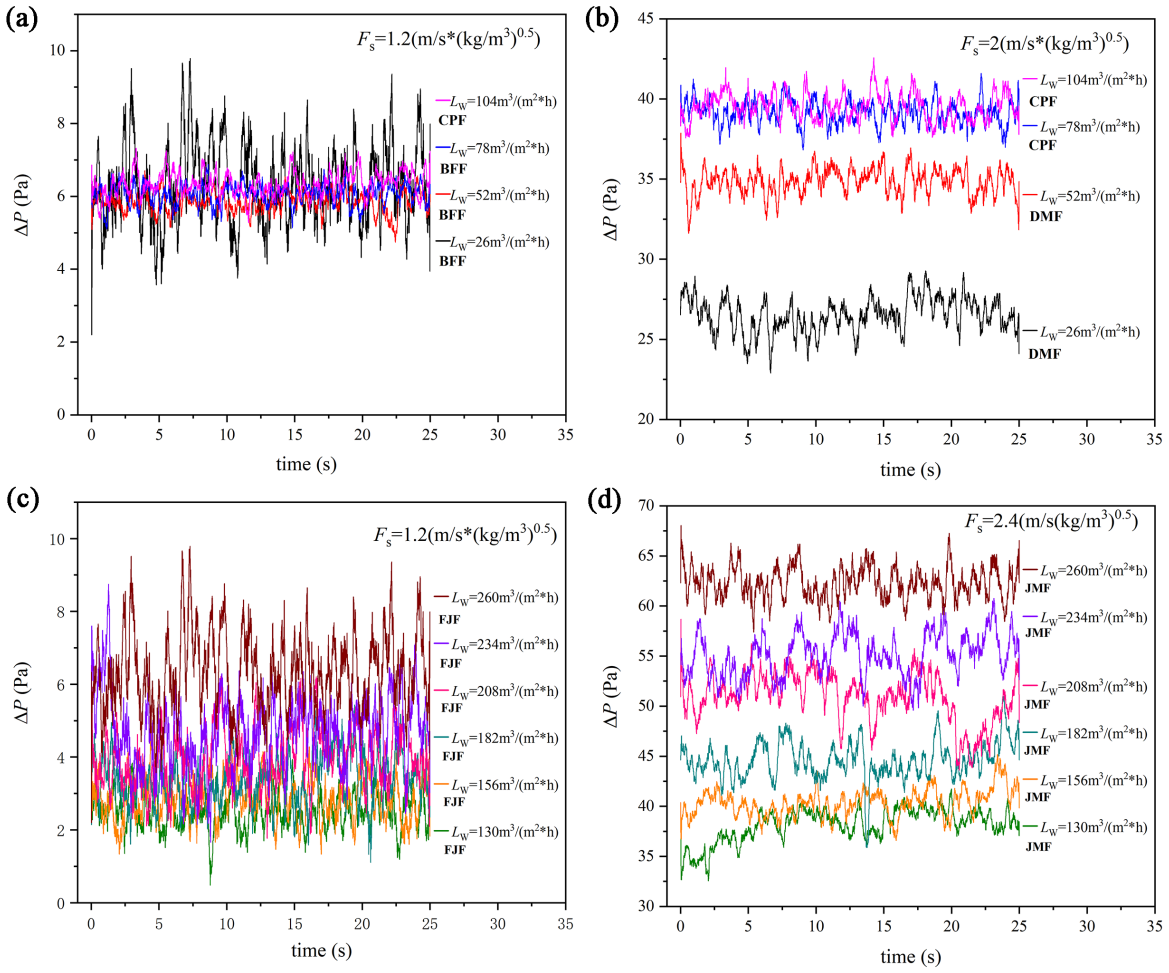

Fig. 10 Time-domain diagram of differential pressure pulsation under different spray densities. (a) F_s= 1.2 (m/s*(kg/m^3)$^{0.5}$) and (b) F_s= 2.0 (m/s*(kg/m^3)$^{0.5}$) in overflow distribution; (c) F_s = 1.2 (m/s*(kg/m^3)$^{0.5}$) and (d) F_s= 2.4 (m/s*(kg/m^3)$^{0.5}$) in spray distribution.

Fig. 10 shows the time-domain diagram of the pulsation signal under different spray densities with the gas-phase kinetic factors F_s = 1.2 (m/s*(kg/m^3)$^{0.5}$) and F_s = 2.0 (m/s*(kg/m^3)$^{0.5}$). In Fig. 10a, the pressure difference amplitude does not increase with the increasing spray density. The fluctuation of the pressure difference decreases as the spray density increases. The flow pattern is changed to a BFF with the spray density of L_W< 104 m^3/(m^2*h). At this point, the gas phase perforated flow is hindered by the liquid layer at the sieve holes. With the decreasing liquid phase spray density, the liquid layer becomes thinner. The blocking effect on the gas-phase flow is weakened, and the influence of the gas flow gradually dominates. The film rupture decreases and condensation film reconstruction increases, resulting in pressure loss. The flow pattern changes into CPF with the spray density of L_W= 104 m^3/(m^2*h). Then, the liquid layer of the unit thickens, and the liquid flow is more stable. The blocking effect of the liquid film on the gas-phase perforated flow

at the sieve holes reaches the maximum, and the proportion of the gas-phase perforation decreases, causing the decrease of pressure difference fluctuation.

As shown in Fig. 10b, the gas-phase kinetic factor increases. The pressure difference first increases with increasing liquid spray density and then stabilizes in the range of 40 Pa. The flow pattern corresponds to the DMF with the liquid spray density of L_W = 26 $m^3/(m^2*h)$. Then, the liquid layer of the sieve holes is dispersed by the airflow. The gas-phase proportion of the perforated flow increases, and the gas-liquid interaction is strong. The pressure difference fluctuates greatly; however, the blocking effect on the gas phase is weak owing to the small liquid spray density. In addition, the pressure amplitude is small. With the liquid spray density of L_W = 52 $m^3/(m^2*h)$, the liquid layer on the surface of the unit thickens, and the flow pattern is unchanged. However, the resistance of the gas-phase perforated flow increases, causing an increase in the pressure difference. When the spray density is L_W > 52 $m^3/(m^2*h)$, the flow pattern changes to CPF. The gas phase of the perforated flow is hindered, and the pressure difference becomes larger. The gas phase is dominated by the rotational flow. The flow becomes stable, and the pressure difference fluctuation gradually decreases.

Fig. 10c, d shows the time-domain diagram of the differential pressure pulsation signal under different liquid spray densities with the gas-phase kinetic factors F_s = 1.2 $(m/s*(kg/m^3)^{0.5})$ and F_s = 2.4 $(m/s*(kg/m^3)^{0.5})$. The pressure difference amplitude increases with the liquid spray density concentrated in the range of 0–10 Pa, and the pressure difference fluctuates greatly. The corresponding flow patterns within the operating range are film and jet flow. Based on the characteristics of the flow type, the spray columns hit the surface of the unit, forming a dispersed liquid film and jet stream. In this process, the liquid phase loses energy during impact, dispersion, convergence, injection, etc., resulting in a strong pressure difference fluctuation. However, the effect on the liquid phase and the pressure difference is small, because of the low velocity of the gas phase.

As shown in Fig. 10d, the gas-phase kinetic factor becomes larger. The pressure difference amplitude increases significantly with the spray density, while the pressure difference fluctuation changes similarly. Under this operation, the flow patterns are converted into JMF, the rate of collapse and reconstruction of the liquid layer above the sieve holes is directly affected by the spray density. The increase in spray density increases the rate of liquid layer reconstruction, which increases the resistance of the gas-phase perforated flow, and the pressure difference becomes larger. Because of the consistent flow

patterns in the operation range, the gas-liquid interaction intensity and pressure difference fluctuation are similar.

3.2.2. Frequency domain analysis for pressure pulsation signal

The distribution of the power spectral density (PSD) under different kinetic energy factors of the gas phase in the overflow and spray distributions are shown in Fig. 11, and the PSD values increase with the gas-phase kinetic factor. According to the characteristics of each flow pattern, under the joint action of the perforated and mixing flow of gas-liquid, the first and second main frequencies and corresponding density values will change correspondingly. The variation of the PSD with the gas-phase kinetic energy factor with a liquid phase spray density of L_W = 78 $m^3/(m^2*h)$ is shown in Fig. 11a. When the spray density is $F_s \leq 1.2$ $(m/s*(kg/m^3)^{0.5})$, the flow pattern is BFF. The main frequencies change in the range of (2.52 Hz–5.28 Hz), and the PSD values change within (0.0040 dB/Hz–0.0070 dB/Hz). The liquid is coated on the surface of the unit, while the gas phase mainly flows through the unit in the form of rotational flow. The gas phase in the perforated flow is minimal, and the mixture strength of the gas phase is lower. The pressure signal carries less energy, and the PSD values are small under each main frequency. For increasing gas kinetic factors, the values of the factor are in the range of 1.6–2.0 $(m/s*(kg/m^3)^{0.5})$. The two main frequencies are slightly reduced, and the PSD values are slightly increased within (0.0098 dB/Hz–0.0226 dB/Hz), corresponding to the main frequencies within (2.48 Hz–4.72 Hz). Then, the flow pattern is transformed into a continuous flow, and the driving force of the gas phase begins to dominate. The gaps in the liquid layer above the sieve holes keep changing alternately. The gas-phase ratio of perforated flow increases, and the perforation flow of the gas-phase and gas-liquid mixing strength become larger. For the gas kinetic factor $F_s > 2.0$ $(m/s*(kg/m^3)^{0.5})$, the flow pattern is dispersion-mixing flow. The frequency range of the main frequencies begins to expand (2.44 Hz–5.4 Hz), and the PSD values increase (0.0098 dB/Hz–0.0226 dB/Hz). The liquid layer on the unit is dispersed by the airflow, which further enhances the renewal frequency of the liquid film, while the droplets on the back of the unit are constantly mixed. The gas-liquid interaction is intense, and the energy of the main frequencies are increased.

The variation of the PSD with gas-phase kinetic factors under the liquid spray density L_W = 156 $m^3/(m^2*h)$ in spray distribution for the liquid phase is shown in Fig. 11b. For factor $F_s \leq 1.6$ $(m/s*(kg/m^3)^{0.5})$, the two main frequencies change in the range of (2.48 Hz–

5.16 Hz), and the PSD varies in (0.0109 dB/Hz–0.0203 dB/Hz). The flow pattern on the unit is FJF. The stability of the liquid layer above the sieve holes is poor, and the perforated flow of the gas phase occupies a certain proportion. At this moment, the velocity of the gas phase is low, and the resistance of perforated flow for the gas phase is large. The perforated strength for the gas phase shows minimal change, and the PSD values of the two main frequencies are more stable within the operating range. For the increasing gas kinetic factor range $F_s \geq 2.0$ (m/s*(kg/m^3)$^{0.5}$), the variation of the two main frequencies expand to the high frequency range (2.36 Hz–5.36 Hz). The PSD values are improved (0.0234 dB/Hz–0.0758 dB/Hz), and sub-peaks appear in the high-frequency range. In this operating range, the flow pattern changes to JMF, and the liquid layer above the sieve holes begins to blow away. The gas-phase perforation strength and two-phase mixing increases, and the flow field is chaotic on the reverse of the unit. Moreover, the frequency energy, number of sub-peaks, and energy for the pressure signal increases significantly with the increasing gas-phase kinetic factors. The gas-liquid contact degree is further strengthened.

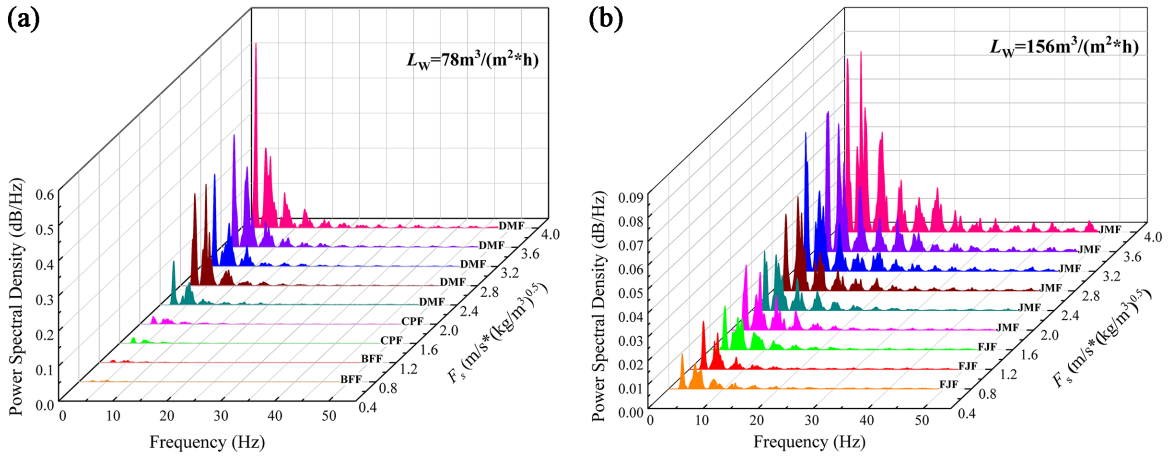

Fig. 11 Distribution diagram of the PSD under different liquid arrangement methods with the gas-phase kinetic factors. (a) L_W = 78 m^3/(m^2*h) in overflow distribution; (b) L_W = 156 m^3/(m^2*h) in spray distribution.

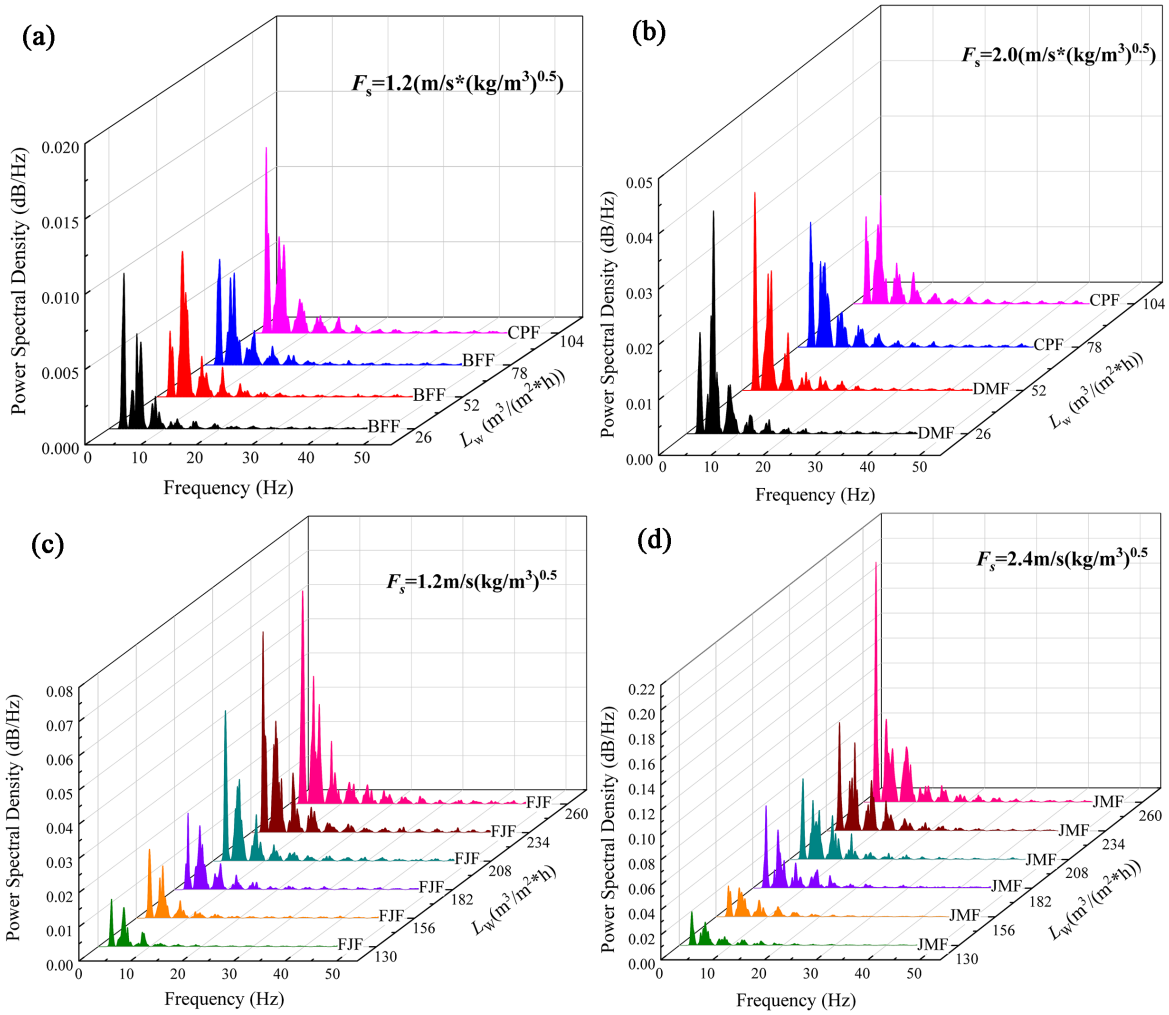

Fig. 12 Distribution diagram of the PSD under different liquid arrangement methods with the liquid spray densities. (a) F_s = 1.2 (m/s*(kg/m^3)$^{0.5}$) and (b) F_s = 2.0 (m/s*(kg/m^3)$^{0.5}$) in overflow distribution; (c) F_s = 1.2 (m/s*(kg/m^3)$^{0.5}$) and (d) F_s = 2.4 (m/s*(kg/m^3)$^{0.5}$) in spray distribution.

Fig. 12a, b shows the PSD distributions with different liquid spray densities under an overflow distribution of the liquid. The gas-phase kinetic factors are F_s = 1.2 (m/s*(kg/m^3)$^{0.5}$) and 2.0 (m/s*(kg/m^3)$^{0.5}$). For the liquid spray density $L_W \leq$ 78 m^3/(m^2*h), the two main frequencies move within (2.36 Hz–5.28 Hz). The PSD value changes in the range (0.0044 dB/Hz–0.0104 dB/Hz) and decreases with the increasing liquid spray densities (see Fig. 12a). At this point, the flow pattern corresponds to BFF. The two-phase flow is more stable, and the rotational flow is dominant. The increase in the proportion of the liquid phase will increase the resistance of the gas phase and consume gas-phase energy, resulting in a decrease in the PSD value. For the increasing spray density L_W = 104 m^3/(m^2*h), the flow pattern is CPF. The liquid layer on the unit is thicker, and the liquid phase perforates out from the sieve holes affected by gravity and the driving force of

airflow. As shown in Fig. 12b, the gas-phase kinetic factor has increased to 2.0 (m/s*(kg/m^3)$^{0.5}$). The liquid spray density is $L_W \leq$ 52 m^3/(m^2*h), and the two main frequencies vary within the range of (2.48 Hz–5.64 Hz), compared with BFF. The PSD value is increased and varies in the range of (0.0184 dB/Hz–0.0403 dB/Hz). At this time, the corresponding flow pattern is DMF. The gas-phase ratio and intensity of the perforated flow is increased. The PSD value for the first main frequency increases. When the spray density continues to increase to $L_W >$ 52 m^3/(m^2*h), the two main frequencies remain unchanged, and the PSD value is within (0.0155 dB/Hz–0.0226 dB/Hz), showing a decreasing trend. Then, the flow pattern is transformed into CPF. The liquid layer above the sieve holes is thickened. The gas-phase perforation channel and intensity strength became smaller. The flow is blocked, resulting in a decrease in the PSD values for the main frequencies.

Fig. 12c, d shows the variations of the PSD values under different liquid spray densities, with the kinetic factors F_s = 1.2 (m/s*(kg/m^3)$^{0.5}$) and 2.4 (m/s*(kg/m^3)$^{0.5}$), under a spray distribution of the liquid phase. As shown in Fig. 12c, the two main frequencies change in the range of (2.36 Hz–5.16 Hz), remaining unchanged with the liquid spray densities, and the PSD values show an increasing trend, ranging from (0.0115 dB/Hz–0.0623 dB/Hz). At this operating condition, the corresponding flow pattern at each liquid spray density is FJF, and the liquid phase plays a leading role. The strength of the liquid jet streams hitting the surface of the unit increases with increasing spray density, which intensifies the gas-liquid mixing. In addition, the interaction of the two phases increases, increasing the energy of the main frequencies. For the increasing gas-phase kinetic factor F_s = 2.4 (m/s*(kg/m^3)$^{0.5}$), the range of the main frequencies is similar to that of FJF. The PSD value increases, ranging from (0.0189 dB/Hz–0.1925 dB/Hz), (see Fig. 12d). The flow pattern changes to JMF, and the perforation intensity is increased. The velocities of the liquid jet streams increase with the spray densities. The liquid phase flow is more disordered. The liquid jet streams hit the surface of the unit, and then, the interaction between the two phases is more intense. The strength of the two phases is increased. The PSD values of the main frequencies are significantly improved. For the liquid phase spray density L_W = 260 m^3/(m^2*h), the turbulence intensity of the gas-liquid phase flow on the unit surface reaches the maximum. The perforated resistance of the gas-phase flow is also the largest, and the interaction intensity of the gas-liquid phase is the strongest within the experimental operating conditions.

3.3 Operating conditions

Combined with the flow pattern image recognition, time domain, and PSD analysis of the differential pressure pulsation signal, in the range of the experimental operating conditions ($0 < F_s \leq 4.0$ (m/s*(kg/m^3)$^{0.5}$), $0 < L_W \leq 260$ m^3/(m^2*h)), the distribution of each flow pattern is shown listed in Table 2.

Table. 2 Distribution of the flow patterns within the operation domain

Gas phase kinetic factor	Liquid phase spray density	Flow pattern
$F_s \leq 1.2$(m/s*(kg/m^3)$^{0.5}$)	$L_W \leq 78$ m^3/(m^2*h)	BFF
$1.2 < F_s \leq 1.6$(m/s*(kg/m^3)$^{0.5}$	$L_W \leq 78$ m^3/(m^2*h)	CPF
$F_s \leq 2.0$ (m/s*(kg/m^3)$^{0.5}$	$78 < L_W \leq 130$ m^3/(m^2*h)	CPF
$F_s > 1.6$ (m/s*(kg/m^3)$^{0.5}$)	$L_W \leq 78$ m^3/(m^2*h)	DMF
$F_s > 1.6$ (m/s*(kg/m^3)$^{0.5}$)	$78 < L_W < 130$ m^3/(m^2*h)	DMF
$F_s \leq 1.6$(m/s*(kg/m^3)$^{0.5}$)	$L_W \geq 130$ m^3/(m^2*h)	FJF
$F_s > 1.6$(m/s*(kg/m^3)$^{0.5}$)	$L_W \geq 130$ m^3/(m^2*h)	JMF

3.4. Distribution of rotational and perforated flow for the gas-liquid phase of the blade unit

The proportion of the gas-liquid rotational and perforated flow on the blade unit affects the hydrodynamics in the unit. In this section, the rotational flow ratio is introduced to study the distribution mechanisms of the rotational and perforated flow for the gas-liquid phase. The rotational flow ratio is divided according to the liquid phase arrangement method in the experiment.

The bottom area of the rotational flow separation chamber is the same as that of the perforated separation chamber. Thus, the liquid rotational flow ratio η_{lr} (liquid rotational flow ratio) can be calculated with the liquid level heights:

$$\eta_{lr} = \frac{h_{lr}}{h_{lr} + h_{lp}} \tag{3}$$

Where the level height of the rotational flow separation chamber is h_{lr}（liquid rotational flow）, and h_{lp} (liquid perforated flow) represents the level height for the perforated flow

separation chamber.

As shown in Fig. 2, the outlets for the gas phase have the same diameter. The gas-phase rotational flow ratio can be calculated with the average velocity of the outlets.

$$\eta_{gr} = \frac{u_{gr}}{u_{gr} + u_{gp}} \tag{4}$$

Here, u_{gr} and u_{gp} are the mean gas velocity for the rotational flow and perforated flow, respectively; $\eta_{gr\text{-}s}$(spray) and $\eta_{lr\text{-}s}$(spray) represent the rotational ratio for the gas and liquid phase under the spray distribution of liquid, respectively, and $\eta_{gr\text{-}o}$ (overflow) and $\eta_{lr\text{-}o}$ (overflow) are the rotational ratio for the gas and liquid phase under overflow distribution, respectively.

3.4.1. Rotational flow ratio in overflow distribution

Fig. 13 shows the variations of the rotational ratio for the gas and liquid phases with the operating conditions. As shown in Fig. 13a, the rotational flow of the gas-phase increases first, then decreases with the increasing gas-phase kinetic factor, and the decreasing trend is larger. For the liquid spray density L_W = 26 $m^3/(m^2*h)$ and the gas-phase kinetic factor $F_s \leq$ 1.6 $(m/s*(kg/m^3)^{0.5})$, the flow pattern corresponds to the BFF, and the sieve holes of the unit are covered by the liquid layer. The resistance for the gas-phase perforated flow is large because of the smaller driving force of the gas phase. Therefore, most of the gas phase flows in rotational flow. Thus, the rotational flow ratio is larger than 0.6. In addition, in this flow pattern, although the gas-phase kinetic factor increases continuously, the driving force of the gas phase cannot break the liquid layer above the sieve holes. Therefore, more gas phase flows in the form of rotational flow, and the rotational flow ratio for the gas phase increases slowly. For the gas-phase kinetic factor $F_s >$ 1.6 $(m/s*(kg/m^3)^{0.5})$, the flow pattern changes to CPF and then changes to DMF with the increasing gas-phase kinetic factor. Under these two flow patterns, the driving force for the gas phase increases gradually, making the liquid layer above the sieve holes flow out in the form of liquid jet streams and dispersed droplets and renew rapidly. During this process, the perforated gas phase increases with the increasing gas phase kinetic energy factor. Thus, the gas-phase rotational flow ratio decreases rapidly. Compared to the perforated flow, the gas-phase rotational flow ratio remains above 0.5 (see Fig. 13a), indicating that the rotational flow for the gas phase occupies a large proportion. For a comparison, the

gas-phase rotational flow ratios at $L_W = 0$ are shown in Fig. 13a. The gas phase rotational flow ratio remains at approximately 0.5 with increasing gas-phase kinetic factor. Thus, under the structure parameters of this blade unit, the gas phase of the swirling and perforated flows account for half of each other. The addition of the liquid phase increases the resistance of the perforated flow for the gas phase and reduces the proportion of the perforated flow. For the range of liquid phase spray density L_W = 52-104 $m^3/(m^2*h)$, the turning point of the rotational flow ratio for the gas phase changes to F_s = 2.0 $(m/s*(kg/m^3)^{0.5})$, corresponding to the transition conditions of the flow pattern.

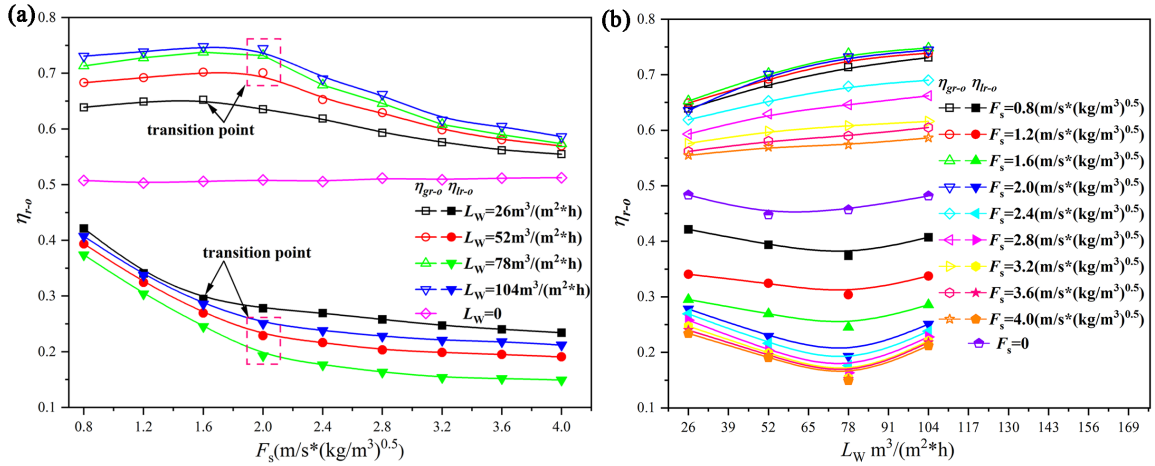

Fig. 13 Variations with (a) gas phase kinetic factor and (b) liquid spray density of the rotational flow ratio for the gas-liquid phase in overflow distribution.

As shown in Fig. 13b, the rotational flow ratio for the gas phase increases slowly with increasing liquid spray density. With the increasing liquid phase spray density, the liquid layer above the sieve holes under all flow patterns gradually thickens, resulting in an increase in the resistance of perforated flow for the gas phase, which decreases the proportion of perforated flow and enlarges the proportion of rotational flow. Therefore, the gas-phase rotational flow ratio increases gradually. The rotational flow ratio for the liquid phase decreases first and then increases with increasing liquid spray density. The turning point is approximately L_W = 78 $m^3/(m^2*h)$ because the flux for the sieve holes is limited. Within the load capacity, the perforated flow for the liquid phase continuously increases, and the rotational flow ratio decreases with increasing spray density. However, after exceeding the capacity of the sieve hole load, the perforation fluid volume reaches its limit, and then, the perforation liquid phase will not increase with increasing spray density. The liquid phase can only flow out in the form of rotational flow. Thus, the rotational flow ratio increases slightly. For a comparison, the rotational flow ratio for the liquid phase with the

gas-phase kinetic factor $F_s = 0$ is shown in Fig. 13b. The rotational flow ratio also decreases first and then increases, slightly less than 0.5. The turning point occurs at L_W = 52 $m^3/(m^2*h)$. Therefore, under the structural parameters of this unit, when only the liquid phase is present, the rotational flow for the liquid phase and the perforated flow also account for roughly half. Increasing the kinetic energy factor of the gas phase will promote the perforation flow of the liquid phase and make the load limit of the sieve holes lag.

3.4.2. Rotational flow ratio in spray distribution

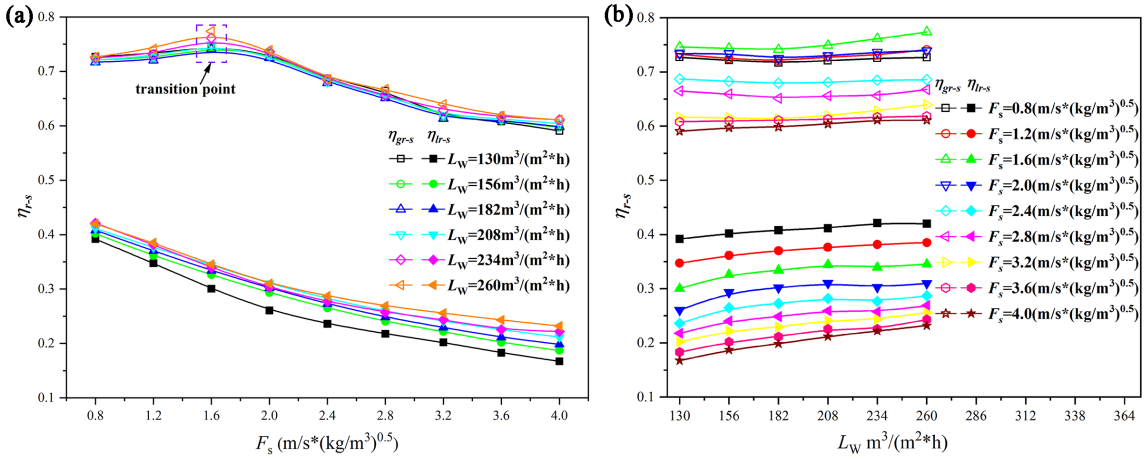

Fig. 14 Variations with (a) gas phase kinetic factor and (b) liquid spray density of the rotational flow ratio for the gas-liquid phase in spray distribution.

Fig. 14a, b shows the variations of the gas-liquid phase rotational flow ratio with the liquid spray density and gas-phase kinetic factor, respectively. In Fig. 14a, the trend of the gas-phase rotational flow ratio with an increasing gas-phase kinetic energy factor is similar to that under the overflow distribution, which increases slightly and then decreases significantly. The ratio is also greater than 0.6, and the action mechanism is similar to that under the overflow distribution. The transition point of the FJF and JMF is F_s = 1.6 $(m/s*(kg/m^3)^{0.5})$, indicating that the transition of the two flow patterns is only affected by the gas phase. However, the liquid rotational flow ratio shows a linear downward trend without a transition because, under the spray distribution, the liquid spray density is large. The liquid phase pushed by the airflow will be supplemented immediately; therefore, the transition of the rotational flow ratio in the two flow patterns is buffered, and the declining trend of the rotational flow ratio for the liquid phase is more stable.

As shown in Fig. 14b, the rotational flow ratio for the gas phase remains unchanged, above 0.6, with the increasing spray density for the liquid phase. The liquid rotational flow ratio shows a slight increase and remains below 0.4 under the spray distribution. Because of

the large liquid phase volume, the gas-liquid phase load at the sieve holes are saturated. The liquid phase cannot produce more perforated flow with the increasing liquid spray density. Only rotational flow is shown, resulting in a gradual increase in the rotational flow ratio of the liquid phase. However, the gas-phase rotational flow ratio is dominated by the gas phase, and the liquid phase has minimal influence. The change is relatively stable.

3.4.3. Prediction model for the rotational flow ratio

A prediction model for the rotational flow ratio is required for the selection and regulation of suitable conditions in future engineering applications. Therefore, the mathematical modeling of the rotational flow ratio of the gas-liquid phase under overflow and spray distribution is carried out in this section.

3.4.3.1. Prediction model in overflow distribution

As previously discussed, the change of the rotational flow ratio is mainly affected by the operating conditions of the gas-liquid phase. To facilitate mathematical modeling, the gas and liquid Reynolds number and Weber number are applied to analyze the changes.

The flow of the liquid phase on the guide plate is falling film flow under the overflow distribution for the liquid phase [32,33]. In addition, the Reynolds number for the liquid phase can be expressed as:

$$Re_{\text{l-o}} = \frac{4\delta u_{\text{m}} \rho_{\text{l}}}{\mu_{\text{l}}}, \tag{5}$$

where the liquid phase density is ρ_{l}; the liquid film thickness is δ; the average velocity for the liquid phase is u_{m}, and the liquid phase dynamic viscosity is μ_{l}.

In the vertical direction, one side of the liquid film is in contact with the guide plate, and the other side is in contact with the atmosphere. The boundary conditions can be expressed as follows.

Guide plate side: $u|_{\text{y=0}} = 0$ (6)

Atmosphere side: $\tau|_{\text{y=}\delta} = \mu \left.\frac{du}{dy}\right|_{\text{y=}\delta} = 0$ (7)

Here, τ is the shear stress in the flow direction, and y is the distance between the calculated point and guide plate.

According to the characteristics of falling film flow and Newton's law of momentum

conservation and shear stress, the velocity distribution equation of the liquid film can be obtained:

$$u=\frac{\rho_{\mathrm{l}} g\delta^2\cos\beta}{2\mu_{\mathrm{l}}}\left(2\frac{y}{\delta}-\left(\frac{y}{\delta}\right)^2\right) \quad , \tag{8}$$

where β is the angle between the inclined plate and vertical direction in the liquid falling film flow. In this experiment, β=0°, and the average velocity of the liquid film can be obtained from the velocity distribution equation.

$$u_{\mathrm{m}}=\frac{1}{\delta}\int_0^{\delta} u dy=\frac{\rho_{\mathrm{l}} g\delta^2\cos\beta}{3\mu_{\mathrm{l}}} \tag{9}$$

In this experiment, the width of the falling film is the same as the width of the guide plate *W*, and the relationship between the liquid film thickness and the liquid volume *L* can be determined by the velocity distribution formula.

$$L=W\delta u_{\mathrm{m}}=\frac{W\rho_{\mathrm{l}} g\delta^3\cos\beta}{3\mu_{\mathrm{l}}} \tag{10}$$

According to equation (10), the liquid film thickness can be obtained as follows.

$$\delta=\sqrt[3]{\frac{3\mu_{\mathrm{l}} L}{\rho_{\mathrm{l}} gW\cos\beta}} \tag{11}$$

Then, equations (11) and (9) are substituted into equation (5) to obtain $Re_{\mathrm{l\text{-}o}}$.

The gas Reynolds number and Weber number can be calculated from equations (12) and (13), respectively.

$$Re_{\mathrm{g}}=\frac{4d_{\mathrm{e}}u_{\mathrm{g}}\rho_g}{\mu_{\mathrm{g}}} \tag{12}$$

Weber number :

$$We=\frac{\rho_{\mathrm{g}}u_{\mathrm{g}}^2 d_{\mathrm{e}}}{\sigma} \tag{13}$$

Here, u_{g} is the superficial velocity of the column; d_e is the hydraulic diameter of the gas phase inlet, which can be calculated according to equations (14) and (15), respectively;

ρ_g is the gas phase density, and σ is the surface tension coefficient between the two phases.

$$u_g = \frac{G}{A} \tag{14}$$

$$d_e = \frac{4A}{C} \tag{15}$$

Here, G is the gas volume; C is the perimeter of the gas infiltration edge; d_e is the hydraulic diameter of the gas-phase inlet, and σ is the surface tension coefficient between the water and air phase.

Taking into account the above parameters, the rotational flow ratio for the gas phase under the condition of overflow distribution can be expressed as follows.

$$\eta_{gr\text{-}o} = f(Re_{l\text{-}o}, Re_g, We) \tag{16}$$

The prediction model of the swirling ratio of the gas phase under the overflow distribution is obtained.

$$\eta_{gr\text{-}o} = \frac{0.423}{1+e^{0.57-\frac{9.416}{We}}} - \frac{0.166}{\left(\frac{Re_{l\text{-}o}}{Re_g}\cdot We\right)^{0.387}} + 0.439 \qquad R^2=0.975 \tag{17}$$

Similarly, the prediction model of the liquid-phase rotational flow can be obtained as follows.

$$\eta_{lr\text{-}o} = 5.28\times10^{-5}\left(\frac{Re_g}{We}\right)^{0.99} + \left(5.10\times10^{-9}Re_{l\text{-}o}^2 - 5.91\times10^{-5}Re_{l\text{-}o}\right) + 0.281 \quad R^2=0.987 \tag{18}$$

3.4.3.2. Prediction model in spray distribution

The contact mode between the liquid phase and blade unit changes under the spray distribution for the liquid phase. Thus, the Reynolds number for the liquid phase is calculated according to the following formula:

$$Re_{l\text{-}s} = \frac{d_0 u_{l\text{-}s}\rho_l}{\mu_l}\ , \tag{19}$$

where d_0 is the hydraulic diameter of the distributor for the liquid phase, which can be calculated as follows.

$$d_0 = \frac{4s_0}{c_0} \tag{20}$$

Here, s_0 is the area of the spray hole, and c_0 is the perimeter of the spray hole. Substituting equation (20) into equation (19), the liquid Reynolds number under the spray distribution can be obtained as follows.

$$Re_{\text{l-s}} = \frac{4s_0 u_{\text{l-s}} \rho_{\text{l}}}{c_0 \mu_{\text{l}}} \tag{21}$$

Because the gas-phase flow pattern under spray distribution remains the same, the Reynolds number for the gas phase and Weber number are consistent with that under the overflow distribution, and the gas-phase rotational flow ratio can be expressed as follows.

$$\eta_{\text{gr-s}} = f(Re_{\text{l-}s}, Re_{\text{g}}, We) \tag{22}$$

The prediction model of the rotational flow ratio for the gas phase under the spray distribution is obtained.

$$\eta_{\text{gr-s}} = \frac{0.605}{1+\text{e}^{-(0.352+\frac{9.039}{We})}} + \frac{1}{6.605+\frac{Re_{\text{l-s}}}{Re_{\text{g}}}} \quad \text{R}^2=0.948 \tag{23}$$

Similarly, the prediction model for the liquid-phase rotational flow ratio is as follows.

$$\eta_{\text{lr-s}} = 0.443\left(1-\frac{0.157}{(\frac{Re_{\text{l-s}}}{Re_{\text{g}}})^{0.697}}\right)We^{-0.114} \quad \text{R}^2=0.985 \tag{24}$$

Fig. 15 shows the calculated and experimental values. The error is controlled within ± 10%. In contrast, the error of the rotational flow ratio is smaller, within ± 5%, which shows that the mathematical model can predict the rotational flow ratio accurately. In addition, the suitable conditions for the prediction model are $2134 < Re_{\text{l-o}} \leq 8536$ ， $2565 < Re_{\text{l-s}} \leq 5131$ ， $2870 < Re_{\text{g}} \leq 14353$， and $0.521 < We \leq 13.021$.

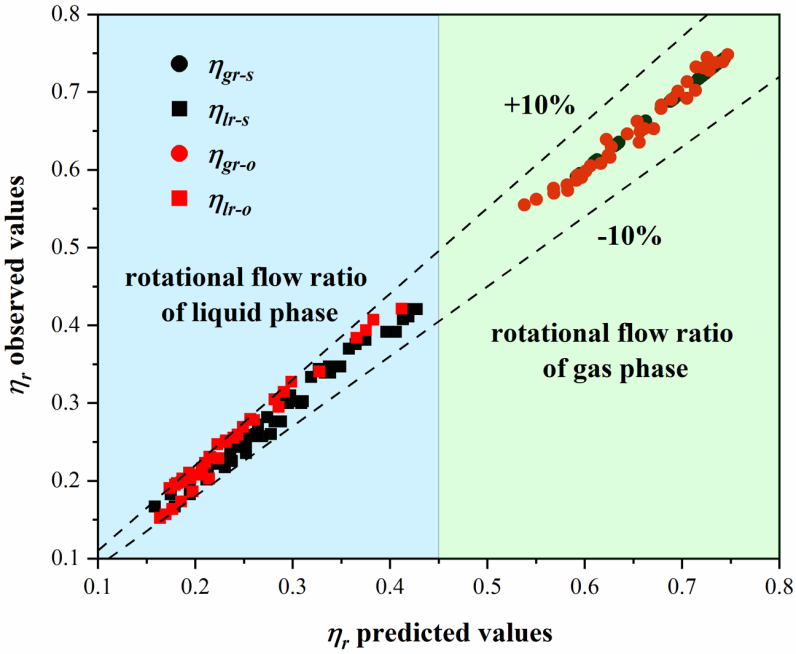

Fig. 15 Rotational flow ratio prediction error diagram

4. Conclusions

A new experimental device is produced, and the hydrodynamics of the blade unit of the tridimensional rotational flow sieve tray are experimentally studied. The flow pattern of the unit under different operating conditions is visually analyzed using the image processing method. The differential pressure pulsation signals under different flow patterns of the blade unit are studied in the time and frequency domain, and the operating domain of the blade unit is clarified. Finally, the distribution of the rotational and perforated flow for the gas-liquid phase, which flows through the blade unit, is measured and analyzed. The following conclusions are obtained.

1) The overflow and spray distributions for the liquid phase are produced according to the liquid phase arrangement methods. Three flow patterns are defined under overflow distribution. They are BFF, CPF, and DMF. Two patterns are defined under spray distribution. They are FJF and JMF.

2) The time and frequency domain analysis for the differential pressure pulsation signals corresponding to each flow pattern is carried out. In the time domain, the increase in the kinetic energy factor of the gas phase will increase the amplitude of the differential pressure signal. When the interaction of the gas-liquid is stronger, the fluctuation of the

differential pressure signal is larger. In the frequency domain under the overflow distribution, the perforation and gas-liquid interaction intensity changes the values of the main frequencies, and the variation range is (2.44 Hz–5.4 Hz). Moreover, when the perforation intensity of the gas phase is higher, the PSD value of the main frequency is higher. The PSD values are affected by the gas-liquid mixing strength, when the liquid arrangement method is the spray distribution. The influence of the airflow on the perforation intensity is weak, and the variations of the main frequency are stable. Finally, the operating range of each flow pattern under the two distribution modes is clarified, according to the changes in the time and frequency domain of the signal, as well as the results of the image observations when the flow pattern changes.

3) A rotational flow ratio is introduced to investigate the distributions of the rotational-perforated flow for the gas-liquid phase. In the experimental operating domain, the gas-phase rotational flow ratio is greater than 0.6, and the liquid-phase is less than 0.5. The gas phase through the blade unit is dominated by the rotational flow, while the liquid phase is perforated flow. The changes in the rotational flow ratio for the gas phase under different liquid arrangement methods are similar. The rotational flow ratio for the gas phase has a turning point when the liquid film is broken by the airflow. The turning point is F_s = 1.6 (m/s*(kg/m^3)$^{0.5}$) (when the arrangement method is overflow distribution: L_W = 26 m^3/(m^2*h), F_s = 2.0 (m/s*(kg/m^3)$^{0.5}$)). Under the overflow distribution, the sieve holes of the blade unit have a limit in the flux for the liquid phase, and the spray density corresponding to the limit will be affected by the gas phase. Finally, a prediction model for the rotational flow ratio under two liquid arrangement methods is proposed, and the error is within ±10%.

Acknowledgment

Funding: This work was supported by the Chinese National Natural Science Foundation [grant number 21776055], Tianjin Enterprise Science and Technology Commissioner Project [grant number 19JCTPJC57900], and the Natural Science Foundation of Hebei Province [grant number B2017202185].

Nomenclature

A= Area of the cross-section of the fluid (m^2)

c_0 = Primeter of the spray hole (m)

C = The perimeter of the gas infiltration edge (m)

d_0 = Hydraulic diameter of the distributor for the liquid phase (m)

d_e = The hydraulic diameter of the gas-phase inlet (m)

e = Universal constant

F_s= Gas-phase kinetic energy factor ($m/s \cdot (kg/m)^{0.5}$)

G = Gas volume flow rate (m^3/h)

h_{lr} = Level height for the rotational flow separation chamber (m)

h_{lp} = Level height for the perforated flow separation chamber (m)

L = Liquid volume flow rate (m^3/h)

L_W = Spray density $m^3/(m^2 \cdot h)$)

R^2 = Correlation coefficient

Re_g = Reynolds number of gas phase

$Re_{l\text{-}o}$ = Reynolds number of liquid-phase in overflow distribution

$Re_{l\text{-}s}$ = Reynolds number of liquid-phase in spray distribution

s_0 = Area of the spray hole

u_g = Superficial gas velocity (m/s)

u_{gp} = Gas velocity of perforated flow (m/s)

u_{gr} = Gas velocity of rotational flow (m/s)

u_m = Average velocity for the liquid phase (m/s)

W = Width of the guide plate (m)

Greek Symbols

η_{gr} = Rotational ratio for the gas phase

$\eta_{gr\text{-}s}$ = Rotational ratio for the gas phase under spray distribution

$\eta_{gr\text{-}o}$ = Rotational ratio for the gas phase under overflow distribution

$\eta_{lr\text{-}s}$ = Rotational ratio for the liquid phase under spray distribution

$\eta_{lr\text{-}o}$ = Rotational ratio for the liquid phase under overflow distribution

δ = Liquid film thickness (m)

ρ_l = Density of liquid phase (kg/m^3)

ρ_g = Density of gas phase (kg/m^3)

σ = Tension coefficient of gas-liquid interface (mN/m)

β = Angle between the inclined plate and vertical direction (°)

ΔP = Pressure drop of blade unit (Pa)

References

1. Li H, Wu Y, Li X, Gao X. State-of-the-Art of Advanced Distillation Technologies in China. *Chemical Engineering & Technology.* 2016;39(5):815-833.

2. Olujić Ž, Jödecke M, Shilkin A, Schuch G, Kaibel B. Equipment improvement trends in distillation. *Chemical Engineering and Processing: Process Intensification.* 2009;48(6):1089-1104.

3. Ratheesh S, Kannan A. Holdup and pressure drop studies in structured packings with catalysts. *Chemical Engineering Journal.* 2004;104(1-3):45-54.

4. Wu H, Buschle B, Yang Y, et al. Liquid distribution and hold-up measurement in counter current flow packed column by electrical capacitance tomography. *Chemical Engineering Journal.* 2018;353:519-532.

5. Soulaine C, Horgue P, Franc J, Quintard M. Gas-liquid flow modeling in columns equipped with structured packing. *AIChE Journal.* 2014;60(10):3665-3674.

6. Rahimi R, Mazarei Sotoodeh M, Bahramifar E. The effect of tray geometry on the sieve tray efficiency. *Chemical Engineering Science.* 2012;76:90-98.

7. Shenastaghi FK, Roshdi S, Kasiri N, Hasan Khanof M. CFD simulation and experimental validation of bubble cap tray hydrodynamics. *Separation and Purification Technology.* 2018;192:110-122.

8. Domingues TL, Secchi AR, Mendes TF. Overall efficiency evaluation of commercial distillation columns with valve and dualflow trays. *AIChE Journal.* 2010;569(9):2323-2330.

9. Wang Q, Chen X, Gong X. Theoretical and experimental investigation on the characteristics of fly-ash scrubbing in a fixed valve tray column. *AIChE Journal.* 2013;59(6):2168-2178.

10. Zhao H, Li L, Wang B, Yu D, Li Q. Hydrodynamics performance and tray efficiency analysis of the novel vertical spray packing tray. *Chinese Journal of Chemical Engineering.* 2018;26(12):2448-2454.

11. Wang H, Niu X, Li C, Li B, Yu W. Combined trapezoid spray tray (CTST)—A novel

tray with high separation efficiency and operation flexibility. *Chemical Engineering and Processing: Process Intensification.* 2017;112:38-46.

12. Zhang M, Zhang BY, Zhao HK, et al. Hydrodynamics and mass transfer performance of flow-guided jet packing tray. *Chemical Engineering and Processing - Process Intensification.* 2017;120:330-336.

13. Liang Z, Rongwong W, Liu H, et al. Recent progress and new developments in post-combustion carbon-capture technology with amine based solvents. *International Journal of Greenhouse Gas Control.* 2015;40:26-54.

14. Liu S, Yang L-l, Zhang D, Xu J-y. Separation characteristics of the gas and liquid phases in a vane-type swirling flow field. *International Journal of Multiphase Flow.* 2018;107:131-145.

15. Xiong Z, Lu M, Wang M, Gu H, Cheng X. Study on flow pattern and separation performance of air–water swirl-vane separator. *Annals of Nuclear Energy.* 2014;63:138-145.

16. Liu L, Bai B. Flow regime identification of swirling gas-liquid flow with image processing technique and neural networks. *Chemical Engineering Science.* 2019;199:588-601.

17. Bao J, Yang L, Sun W, Geng J, Yan J, Shen X. Removal of fine particles by heterogeneous condensation in the double-alkali desulfurization process. *Chemical Engineering and Processing: Process Intensification.* 2011;50(8):828-835.

18. Javed KH, Mahmud T, Purba E. Enhancement of Mass Transfer in a Spray Tower Using Swirling Gas Flow. *Chemical Engineering Research and Design.* 2006;84(6):465-477.

19. Schubert M, Piechotta M, Beyer M, Schleicher E, Hampel U, Paschold J. An imaging technique for characterization of fluid flow pattern on industrial-scale column sieve trays. *Chemical Engineering Research and Design.* 2016;111:138-146.

20. Vishwakarma V, Schubert M, Hampel U. Assessment of separation efficiency modeling and visualization approaches pertaining to flow and mixing patterns on distillation trays. *Chemical Engineering Science.* Aug 10 2018;185:182-208.

21. Qiao M, Wei W, Huang W, Li J, Xue Y, Deng C. Flow patterns and hydrodynamic model for gas-liquid co-current downward flow through an orifice plate. *Experimental Thermal and Fluid Science.* 2019;100:144-157.

22. Maidana NdC, Rosa ES. Flow disturbances induced by an orifice plate in a horizontal air-water flow in the slug regime. *Experimental Thermal and Fluid Science.*

2018;94:59-76.

23. Iliuta I, Larachi F, Fourati M, Raynal L, Roig V. Flooding limit in countercurrent gas–liquid structured packed beds—Prediction from a linear stability analysis of an Eulerian two-fluid model. *Chemical Engineering Science.* 2014;120:49-58.

24. Raynal L, Ballaguet J-P, Barrere-Tricca C. Determination of mass transfer characteristics of co-current two-phase flow within structured packing. *Chemical Engineering Science.* 2004;59(22-23):5395-5402.

25. Tang M, Zhang S, Wang D, Liu Y, Zhang Y. CFD simulation and experimental study of dry pressure drop and gas flow distribution of the tridimensional rotational flow sieve tray. *Chemical Engineering Research and Design.* 2017;126:241-254.

26. Tang M, Zhang S, Wang D, Liu Y, Wang L, Liu C. Experimental study and modeling development of pressure drop in concurrent gas-liquid columns with a tridimensional rotational flow sieve tray. *Chemical Engineering Science.* 2018;191:383-397.

27. Tang M, Zhang S, Wang D, et al. Hydrodynamics of the tridimensional rotational flow sieve tray in a countercurrent gas-liquid column. *Chemical Engineering and Processing - Process Intensification.* 2019;142:107568.

28. Tang M, Zhang S, Wang D, et al. CFD simulation of gas flow field distribution and design optimization of the tridimensional rotational flow sieve tray with different structural parameters. *Chemical Engineering Science.* 2019;201:34-49.

29. Tchowa Medjiade W, Rosenbaum Alvaro A, Schumpe A. Flow regime transitions in a bubble column. *Chemical Engineering Science.* 2017;170:263-269.

30. Gao H, Gong X, Hu G. Statistical and frequency analysis of pressure fluctuation in an annular spouted bed of coarse particles. *Powder Technology.* 2017;317:216-223.

31. Liu H, Zhu Y, Pei S, et al. Flow regime identification for air valves failure evaluation in water pipelines using pressure data. *Water Research.* Nov 15 2019;165:115002.

32. Hu P, Huang X, Bao K, Zhu G. Experiment study on film width and thickness of free falling water film on a large inclined plate. *Nuclear Engineering and Design.* 2020;358:110445.

33. Jayakumar A, Balachandran A, Mani A, Balasubramaniam K. Falling film thickness measurement using air-coupled ultrasonic transducer. *Experimental Thermal and Fluid Science.* 2019;109:109906.